

Fusion of sensor geometry into additive strain fields measured with sensing skin

Austin Downey^{1,2}, Mohammadkazem Sadoughi¹, Simon Laflamme^{2,3}, and Chao Hu^{1,3}

1 Department of Mechanical Engineering, Iowa State University, Ames, IA, USA;

2 Department of Civil, Construction, and Environmental Engineering, Iowa State University, Ames, IA, USA;

3 Department of Electrical and Computer Engineering, Iowa State University, Ames, IA, USA;

E-mail: adowney2@iastate.edu

March 2018

Abstract.

Recently, numerous studies have been conducted on flexible skin-like membranes for the cost effective monitoring of large-scale structures. The authors have proposed a large-area electronic consisting of a soft elastomeric capacitor (SEC) that transduces a structure's strain into a measurable change in capacitance. Arranged in a network configuration, SECs deployed onto the surface of a structure could be used to reconstruct strain maps. Several regression methods have been recently developed with the purpose of reconstructing such maps, but all these algorithms assumed that each SEC measured strain located at its geometric center. This assumption may not be realistic since an SEC measures the average strain value of the whole area covered by the sensor. One solution is to reduce the size of each SEC, but this would also increase the number of required sensors needed to cover the large-scale structure, therefore increasing the need for the power and data acquisition capabilities. Instead, this study proposes an algorithm that accounts for the sensor's strain averaging feature by adjusting the strain measurements and constructing a full-field strain map using the kriging interpolation method. The proposed algorithm fuses the geometry of an SEC sensor into the strain map reconstruction in order to adaptively adjust the average kriging-estimated strain of the area monitored by the sensor to the signal. Results show that by considering the sensor geometry, in addition to the sensor signal and location, the proposed strain map adjustment algorithm is capable of producing more accurate full-field strain maps than the traditional spatial interpolation method that considered only signal and location.

Keywords: structural health monitoring, capacitive-based sensor, soft elastomeric capacitor, flexible membrane sensor, additive strain maps, full-field strain maps, sensor fusion

1. Introduction

Recent advances in sensor technologies have reduced the costs associated with the instrumentation of large-scale (or mesoscale) structures, including civil, aerospace, and energy structures, for structural health monitoring applications [1]. This reduction in cost enables the deployment of distributed dense sensor networks for direct damage sensing over large surfaces. Direct sensing is generally considered to be one of the two categories of methods used for the detection and localization of damage, with the other category being the indirect methods [2]. Indirect sensing technologies (e.g. accelerometers) and methods involve the measurement of a structure's global condition through an often sparse array of sensors. However, the likelihood that a local damage will directly affect the signal output of a sensor is low. As a consequence, these methods rely on sophisticated data analysis and damage detection algorithms. Indirect sensing technologies can be sensitive to, and their application limited by, noisy measurements, complex structures, and/or environmental variations (e.g. humidity and thermal) [3, 4]. In contrast, direct sensing methods involve the deployment of distributed dense sensor networks that are capable of directly inferring damage from a change in a signal with only simple, often called "threshold" algorithms [5]. Examples of strain-based direct damage sensing technologies include fiber-optic sensors, vibrating wire, and resistive strain gauges (RSGs). To provide a structure with a high probability of detection for cracks and other strain field anomalies, a large number of individual sensors are required [2, 6, 7, 8]. While mature technologies such as fiber-optic sensors or vibrating wires can be spatially distributed to increase their damage detection resolution, their relatively high costs (including sensors, data acquisition (DAQ), and installation) and relative bulkiness [9] when mounted on the surface of a structure make them less suited for the monitoring of mesoscale structures [4, 10].

The need for spatially distributed strain sensing technologies has been recognized by multiple researchers and addressed using various techniques. One such technique is electrical impedance tomography (EIT) where either the electrical conductivity, permittivity, or impedance is inferred from the electrical measurements made on the surface of a structure. These measurements are then used to generate a tomographic image of the component. EIT has been used for damage detection in structures by measuring the electrical changes in carbon nanotube skins [11, 12], copper doped conductive paints [13, 14], or through the component itself [15]. While EIT is capable of producing a relatively high spatial resolution, it requires a high contact density and repeated measurements to solve the tomography mapping's inverse problem. In addition, as the analytical solution for the inverse mapping problem is difficult (or sometimes impossible) to formulate, the

finite element or finite difference method must be used to obtain an approximate solution [16]. Despite high spatial resolution capabilities, the requirements for repeated measurements using a variety of contacts and for solving the inverse mapping problem make the EIT technique not well suited for every application. Another electrical tomography technique uses a resistor mesh model to detect and localize damage-induced strain changes in cement doped with multi-walled carbon nanotubes [17]. However, this model-assisted approach requires that damage be located through the use of a searching method that updates the resistor mesh model associated with the structure, thus adding a relatively high computational cost to the approach [18]. Another notable method to collect spatially distributed strain data is the use of optical measurements (e.g. cameras and photocells) leveraging either digital image correlation [19] or photoactive nanocomposites that generate small amounts of light when various levels of strain are reached [20]. While these measurement systems benefit from their being non-contact methods, their requirement of having either a camera or photocell set back from the structure limits their deployment in some applications.

The use of large area electronics or sensing skins for the condition assessment of structures is an emerging technology enabling a broad range of sensors and their associated electronics to be integrated onto a single sheet [21, 22]. These sensing skins allow for the easy installation of a high number of discrete sensors over a large-scale surface. The discrete sensors that make up a sensing skin allow for the direct detection and localization of damage. These sensing skins are analogous to biological skin in that they are capable of detecting and localizing damage over a structure's global area. Various researchers have proposed sensing skins that are self-contained units, with all the sensing, data acquisition, power harvesting, and communications built onto a single flexible sheet. Numerous examples of sensing skins, at various stages of development, have been tested at the laboratory scale. One example is a sensing skin that uses a plurality of traditional RSGs and integrated circuits mounted onto a single flexible substrate [23]. A prototype of this RSG based sensing skin was fabricated where communications between the sensors and integrated circuits was done through conductive and capacitive antennas to provide a low-cost and scalable architecture [24]. Other researchers have looked at using polymer materials doped with carbon nanotubes to form piezoresistive strain sensors [25, 26, 27] that could be combined with electronics to constitute sensing skins. One such example is a fully integrated sensing skin that combined thin film resistive sensors fabricated from a carbon nanotube composite with the required electronics for on-board resistance measurements [28]. Other promising approaches for the realization of large-scale sensing skins include using a CO₂ laser to directly write RSGs onto a polyimide film to form graphitic porous sensor arrays that

could be easily customizable in shape and size [29] and the use of strain sensors printed with conductive ink [30].

Another sensing skin, being developed by the authors of this paper, is based on a densely deployed network of low-cost large area capacitor termed the soft elastomeric capacitor (SEC) [31]. The SEC is a robust and durable sensor [32] that is customizable in both shape and size. One particularly useful attribute of the SEC is its capability to measure the additive strain of a structure ($\epsilon_x + \epsilon_y$) [31]. The individual SEC has been characterized for both its static [33] and dynamic [34] behaviors. The sensing skin consisting of a network of SEC sensors has been used for the generation of full-field uni-directional strain maps [35, 36], and for the detection of fatigue cracks in steel bridges [37]. Additionally, an SEC-based sensing skin has been studied for the detection and localization of damage on a wind turbine blade, both numerically [38] and experimentally [39].

Because the SEC is a strain transducing sensor, it follows that a network of SECs deployed onto the surface of a structure could be used to reconstruct strain maps. An approximated full-field additive strain map can be reconstructed by assuming that the measurement of each SEC is located in the geometric center of the SEC and interpolating the measurement points between adjacent SECs. Various interpolation methods can be used for this task, including radial basis functions [40], cubic splines [41], and kriging (or Gaussian process regression) [42]. As the number and density of SECs deployed over a given area increases, the approximated full-field strain map will become more accurate due to the capability of the SEC network to reproduce more complex strain topographies. However, as with any sensing technology, an increase in the number of sensors deployed onto a structure necessitates increased power, data acquisition capabilities, and communication hardware. Therefore, a trade-off must be made between the cost (economic and technical) associated with a particular sensor density and the required strain map resolution. To help reduce the severity of this trade-off, this work introduces a robust algorithm that fuses the geometry (i.e. the area of the sensor) of the SEC sensor into the previously discussed strain map interpolation method that relied solely on the sensor signal and sensor location.

The strain map adjustment algorithm works by first building a traditional full-field strain map using the SEC sensor signals and locations and then interpolating the measurement points between the sensors. In this work kriging is used as the interpolation method. Next, the sensor geometry is fused into the strain map by calculating what the signal of each SEC should be using the kriging-estimated strain map under the area covered by each sensor and adjusting the SEC signal used for training the kriging model. Thereafter, the computation iteratively adjusts the SEC signal used for training the kriging model

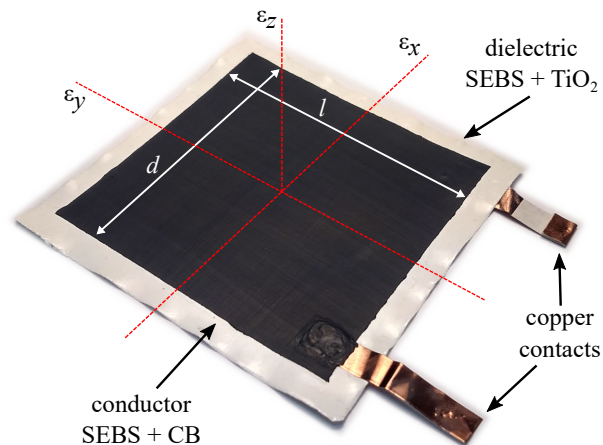


Figure 1. An SEC sensor with key components, dimensions, and axes annotated.

until the estimated signal from the kriging-derived strain map converges to the actual signal of the SECs. The improvement in full-field strain estimation allows for more accurate damage and strain field anomaly detection. In cases where uni-directional strain maps are needed, this algorithm can be used to improve the accuracy of the additive strain field used in the decomposition task using a previously proposed kriging-based [35] or least-squares-based [36] algorithm. Results show that by considering the sensor geometry, in addition to the sensor signal and location, the proposed strain map adjustment algorithm is capable of producing more accurate full-field strain maps with a given number of sensors than the traditional interpolation method that considered only the sensor signal and location.

2. Background

This section provides a brief review of the SEC sensor that forms the basis of the SEC-based sensing skin, followed by a brief introduction to the kriging method used in this work.

2.1. Soft Elastomeric Capacitor

The Soft Elastomeric Capacitor (SEC) is a highly scalable thin-film strain sensor. Figure 1 presents a square SEC with a area of 56 cm². The sensor is a parallel plate capacitor with its strain sensing principle derived from the fact that a change in area (i.e., strain) of the monitored structure will provoke a measurable change in its capacitance. The fabrication process of the SEC is simple and highly scalable, because it does not require any highly specialized manufacturing or processing equipment. The dielectric of the capacitor is constituted from an SEBS block co-polymer filled with TiO₂ to increase both its durability [32, 43] and permittivity [44]. The conductive layers painted onto each side of the SEC sensor are fabricated by doping

Algorithm 1 Pseudocode for the strain map adjustment algorithm

-
- 1: Build and run the initial kriging model.
 - 2: Use the kriging model to calculate the estimated SEC signal.
 - 3: Calculate the difference between the SEC signal and the kriging model's estimated SEC signal.
 - 4: **while** difference > difference threshold **do**:
 - 5: Add the difference to the SEC signal.
 - 6: Build and run the updated kriging model.
 - 7: Use the updated kriging model to calculate the estimated SEC signal.
 - 8: Calculate the difference between the SEC signal and the kriging model's estimated strain.
 - 9: **end while**
 - 10: Build the final kriging model based on the adjusted SEC signal.
 - 11: Run the final kriging model to develop improved additive strain maps.
-

199 the same SEBS but filled carbon black instead of TiO₂.
 200 Carbon black is used as the conductive filler as it allows
 201 for conductive pathways to form within the SEBS matrix.
 202 Additionally, it absorbs both UV and visible light [45] and
 203 has demonstrated resiliency to weathering [32]. Currently,
 204 electrical connections are made to the painted conductive
 205 layers of the SEC using copper contacts. To ensure a good
 206 connection between the copper contact and SEBS-based
 207 conductive paint, a thin layer of the conductive paint is
 208 added on top of the copper contacts as denoted in Figure
 209 1. For more details regarding the manufacturing process of
 210 the SEC sensors, the interested reader is referred to [31, 34].

211 An electro-mechanical model that relates a change in
 212 area of the monitored structure to a measurable change in
 213 capacitance can be derived by taking the capacitance (C) of
 214 a parallel plate capacitor, modeled as a non-lossy parallel
 215 plate capacitor:

$$216 \quad C = \epsilon_0 \epsilon_r \frac{A}{h} \quad (1)$$

217 where $\epsilon_0 = 8.854$ pF/m is the vacuum permittivity, ϵ_r is
 218 the polymer's relative permittivity, $A = d \cdot l$ is the sensor
 219 area of width d and length l (as annotated in Figure 1), and
 220 h is the thickness of the dielectric. Assuming small strains,
 221 equation (1) can be written as a change in capacitance (ΔC):

$$222 \quad \frac{\Delta C}{C} = \frac{\Delta d}{d} + \frac{\Delta l}{l} - \frac{\Delta h}{h} \quad (2)$$

223 where it can be noted that $\Delta d/d$, $\Delta l/l$, and $\Delta h/h$, can be
 224 expressed as strain components ϵ_x , ϵ_y , and ϵ_z , respectively.
 225 Assuming a plane stress condition, $\epsilon_z = -\nu/(1-\nu) \cdot (\epsilon_x + \epsilon_y)$,
 226 a relative change in capacitance ΔC can be related to a
 227 change in the sensor's deformation as:

$$228 \quad \frac{\Delta C}{C} = \lambda(\epsilon_x + \epsilon_y) \quad (3)$$

229 where ν is the sensor material's Poisson's ratio taken as
 230 $\nu \approx 0.49$ [46]. Therefore, $\lambda = 1/(1-\nu) \approx 2$ represents
 231 the gauge factor of the sensor. A key advantage of the SEC
 232 is its capability to measure the additive strain of a structure,
 233 as shown in equation (3).

2.2. Kriging (Gaussian Process Regression) 234

235 Kriging (or Gaussian process regression) is a statistical 235
 236 process in which interpolated values are obtained from a 236
 237 spatially dependent set of training data. As a general rule, 237
 238 kriging seeks to predict the value of a function at the point 238
 239 of interest by computing a spatially weighted average of the 239
 240 training points in the neighborhood [42, 47]. The spatial 240
 241 variability of a generalized spatially continuous process at 241
 242 a location x , denoted as $\mathbf{Z}(x)$, can be represented as: 242

$$243 \quad \mathbf{Z}(x) = \mu(x) + \epsilon(x) \quad (4)$$

244 where $\mu(x)$ is the mean value of the process and $\epsilon(x)$ deals 244
 245 with the small-scale spatial variation in the process. When 245
 246 considering a noisy process, $\epsilon(x)$ is typically related to 246
 247 the noise (i.e. error) term. In cases where the prediction 247
 248 mean $\mu(x)$ varies smoothly, universal kriging (sometimes 248
 249 called kriging with external drifts or regression kriging) 249
 250 is preferred [48]. When considering external drifts and 250
 251 expressing n observations (training points) as $z(x_1)$, $z(x_2)$, 251
 252 ..., $z(x_n)$, the value at a new, unsampled location x_0 can be 252
 253 predicted as the sum of the drift component (\hat{m}) plus the 253
 254 residual ($\hat{\epsilon}$): 254

$$255 \quad \hat{z}(x_0) = \hat{m}(x_0) + \hat{\epsilon}(x_0) \quad (5)$$

256 where the drift term \hat{m} is fit onto an assumed trend term 256
 257 using linear regression. Various trend terms have been used 257
 258 to model the large-scale spatial variations in the sample 258
 259 data and these terms include linear, polynomial, and point 259
 260 logarithmic [49]. This work uses a regional linear trend to 260
 261 estimate the mean value at x_0 [50]. The universal kriging 261
 262 predicted value $\hat{z}(x_0)$ can be solved for in a matrix notation 262
 263 as: 263

$$264 \quad \hat{z}(x_0) = \mathbf{q}_0^T \cdot \hat{\boldsymbol{\beta}} + \boldsymbol{\lambda}_0^T \cdot \mathbf{e} \quad (6)$$

265 where \mathbf{q}_0 is a vector of the predictors at x_0 , $\hat{\boldsymbol{\beta}}$ is a vector that 265
 266 contains the estimated drift term coefficients, $\boldsymbol{\lambda}_0$ is a vector 266
 267 of n kriging weights determined by the covariance function, 267
 268 and \mathbf{e} is a vector that contains all the regression residuals. 268
 269 The unknown drift term coefficients, $\hat{\boldsymbol{\beta}}$, can be solved for 269

270 using the generalized least squares technique, formulated
271 as:

$$272 \hat{\boldsymbol{\beta}} = (\mathbf{q}^T \cdot \mathbf{C}^{-1} \cdot \mathbf{q})^{-1} \cdot \mathbf{q}^T \cdot \mathbf{C}^{-1} \cdot \mathbf{z} \quad (7)$$

273 where \mathbf{q} is the matrix of the predictors at all observed
274 locations, \mathbf{z} is the sampled observations, and \mathbf{C} is the
275 covariance matrix of residuals:

$$276 \mathbf{C} = \begin{bmatrix} C(x_1, x_2) & \cdots & C(x_1, x_n) \\ \vdots & \ddots & \vdots \\ C(x_n, x_1) & \cdots & C(x_n, x_n) \end{bmatrix} \quad (8)$$

277 The covariance between point pairs $C(x_i, x_j)$, sepa-
278 rated by a distance d , in the covariance matrix are then es-
279 timated using a variogram model. Different forms of vari-
280 ogram models (variance functions) have been developed to
281 model the spatial correlation in the random space between
282 point pairs. Examples of variogram models include the
283 Gaussian, exponential, spherical, linear and power models.
284 For the purpose of this work, the power model was selected
285 due to its simplicity and capability to estimate unbounded
286 spatial variances [51]. The power variogram model is ex-
287 pressed as $s \cdot d^\alpha + n$, and used to form the piecewise semi-
288 variance function $\gamma(d)$:

$$289 \gamma(d) = \begin{cases} 0 & d = 0 \\ s \cdot d^\alpha + n & 0 \leq d \end{cases} \quad (9)$$

290 where s is a scaling factor, α is the exponent (between 1
291 and 1.99), and n is the nugget term [50]. The nugget term
292 accounts for the “noise” in the measurement as it represents
293 the random deviations from the otherwise smooth spatial
294 data trend. $\gamma(d)$ is related with the covariance function for
295 a point wise pair as $\gamma(d) = n - C(x_i, x_j)$. As represented
296 in Equation 9, this work considers measurements that are
297 “exact”, meaning that at the training points the variogram
298 is forced to be zero (i.e. the predicted values at the
299 training points will be equal to the observed values at
300 these points). Lastly, considering that the generalized least
301 squares accounts for the spatial correlation of residuals,
302 Equation 6 can be expressed as:

$$304 \hat{z}(x_0) = \mathbf{q}_0^T \cdot \hat{\boldsymbol{\beta}} + \boldsymbol{\lambda}_0^T \cdot (\mathbf{z} - \mathbf{q} \cdot \hat{\boldsymbol{\beta}}) \quad (10)$$

305 Given that various points of interest are sampled with
306 sufficient density, the universal kriging process outlined
307 here can create a near continuous interpolation of a sampled
308 process. More details about the kriging model can be found
309 in reference [50]. This work utilized PyKrige, an open
310 source kriging toolkit for Python, for the development and
311 solving of the universal kriging interpolation models [52].

312 3. Strain map adjustment algorithm

313 The use of traditional interpolation methods (including
314 kriging and radial basis functions) for the estimation of full-
315 field strain maps for structures monitored by an SEC-based

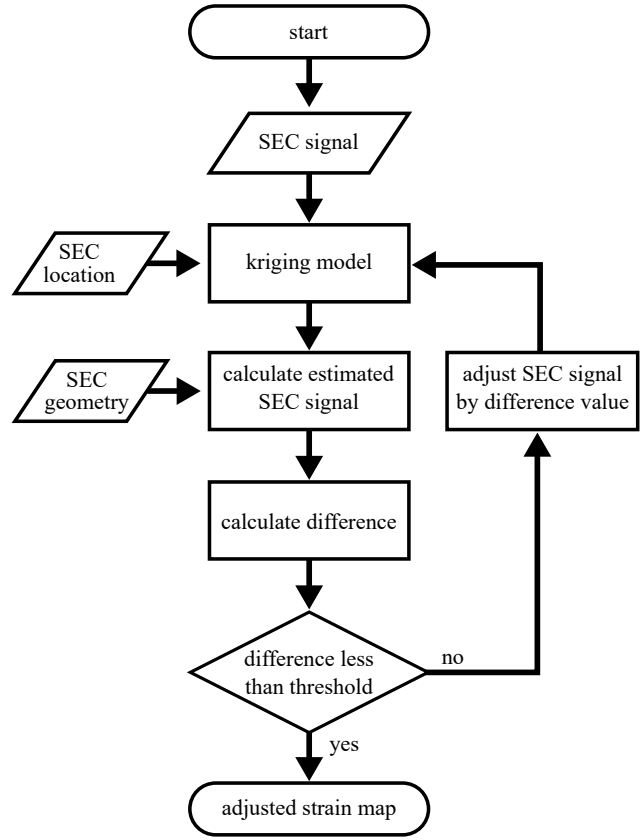


Figure 2. Flowchart detailing the strain map adjustment algorithm.

316 sensing skin only considers the sensor location and signal.
317 For these interpolation methods, the signal of each SEC
318 is deemed to be located at the center of the sensor. The
319 proposed strain map adjustment algorithm improves the
320 accuracy of the full-field strain maps by fusing the sensor
321 geometry, along with the sensor location and signal, into
322 the strain maps.

323 The proposed algorithm maintains the assumption that
324 the signal of the SEC is located at the center of the
325 SEC. However, the additive strain measured by the sensor
326 corresponds to the average strain under the sensing area,
327 and is therefore not equal to the additive strain found at
328 the center. It should also be noted that the discrepancy between
329 these two values increases with either an increase in sensor
330 size or an increase in strain map complexity. The proposed
331 strain map adjustment algorithm is presented as a flowchart
332 in figure 2, described as a pseudocode in algorithm 1, and
333 discussed it what follows. First, a universal kriging model,
334 denoted as UK in the following equations, is trained using
335 the SEC sensor locations \mathbf{I}^{SEC} and their measured additive
336 strain data \mathbf{O}^{SEC} :

$$337 \varepsilon(x, y) = UK((x, y) | \mathcal{D} = \{\mathbf{I}^{\text{SEC}}, \mathbf{O}^{\text{SEC}}\}) \quad (11)$$

338 where $\varepsilon(x, y)$ is the additive strain at an arbitrary point (x, y) .
339 The Gaussian process or kriging model for this arbitrary
340 point is denoted $UK((x, y) | \mathcal{D})$ where \mathcal{D} is the data set used

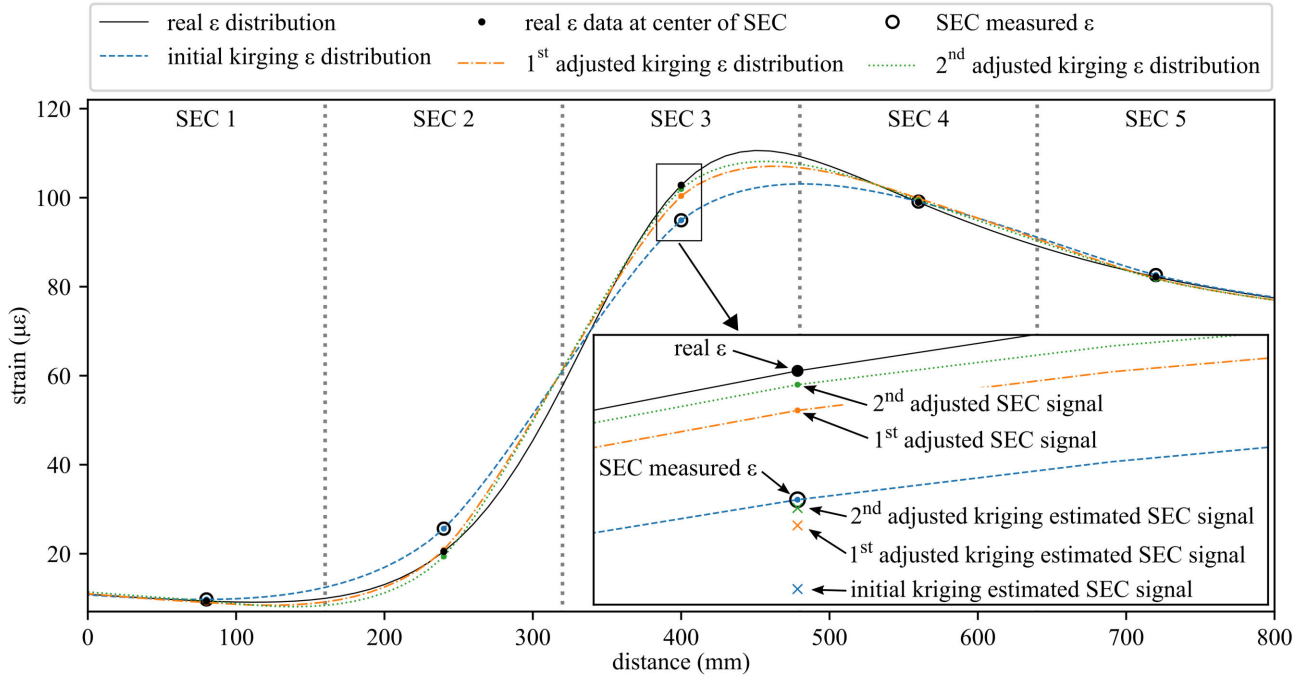


Figure 3. Graphical representation of the first three iterations of the strain map adjustment algorithm for a 1-D pseudo strain data monitored by 5 SECs with the inset showing a closeup of SEC 3.

341 for training the model. Considering an SEC sensor location
 342 i , the average strain value for the area monitored by the
 343 sensor, written as $O_i^{\text{SEC,estimated}}$, is extracted from the 2-D
 344 additive strain field $\varepsilon(x, y)$ such that:

$$345 \quad O_i^{\text{SEC,estimated}} = \frac{1}{n} \sum_{z=1}^n \varepsilon(x_z, y_z) \quad (12)$$

346 where n is the number of strain points under the SEC
 347 sensor i that are sampled from the kriging model. Next,
 348 the difference between the measured strain for a sensor
 349 (O_i^{SEC}) and the strain estimated by the kriging model at that
 350 location ($O_i^{\text{SEC,estimated}}$) is given by:

$$351 \quad \xi_i = O_i^{\text{SEC}} - O_i^{\text{SEC,estimated}} \quad (13)$$

352 Once ξ_i has been solved for, it is used to update the strain
 353 value measured by the sensor (O_i^{SEC}) and create an adjusted
 354 SEC signal value:

$$355 \quad O_i^{\text{SEC,adjusted}} = O_i^{\text{SEC}} + \xi_i \quad (14)$$

356 Combining $O_i^{\text{SEC,adjusted}}$ for all sensors in the sensing skin
 357 yields the vector $\mathbf{O}^{\text{SEC,adjusted}}$. These adjusted strain values,
 358 resulting from a fusion of SEC signals, locations, and
 359 geometries, are used to train a new kriging model:

$$360 \quad \varepsilon(x, y) = UK\left((x, y) | \mathbf{D} = \{\mathbf{I}^{\text{SEC}}, \mathbf{O}^{\text{SEC,adjusted}}\}\right) \quad (15)$$

361 and therefore, a new additive strain field $\varepsilon(x, y)$. This
 362 process of obtaining estimated SEC strain signals from the
 363 kriging-estimated strain field, adjusting the SEC signals

364 based on the difference between the real and estimated
 365 signals, and resolving the kriging-estimated strain field
 366 based on the adjusted signals is repeated until a stop
 367 condition is met. In this work, the stop condition requires
 368 every ξ_i to fall below $0.1 \mu\epsilon$.

369 A graphical representation of the strain map adjust-
 370 ment algorithm for a simplified 1-D case is presented in
 371 figure 3. This 1-D pseudo strain data was created to rep-
 372 resent a relatively complex strain topography that is moni-
 373 tored by five SECs. The measurement of each SEC is the
 374 mean strain over the area monitored by the SEC. The real
 375 strain distribution is represented by the thin black line with
 376 the real strain value at the center of the SEC denoted by
 377 the filled black circles. The geometric transition from one
 378 SEC to another is denoted by the dotted vertical line. The
 379 strain map adjustment algorithm starts with the strain value
 380 measured by the i^{th} SEC from the real strain distribution to
 381 form the data point O_i^{SEC} . For the purpose of this simplified
 382 1-D case, this measurement is obtained without consider-
 383 ing any noise in the signal and is represented by the hollow
 384 black circle in figure 3. These strain measurements can be
 385 observed to correctly estimate the strain value at the center
 386 of the sensor for sensor locations that monitor linear strain
 387 distributions (i.e. SECs 1, 4, and 5) while either overesti-
 388 mating or underestimating the strain value for locations that
 389 monitor more complex strain distributions (i.e. SECs 2 and
 390 4). Once the SEC measurements have been obtained, a krig-
 391 ing model is generated that uses the SEC-measured strain as
 392 the input for the model, this model is then densely sampled

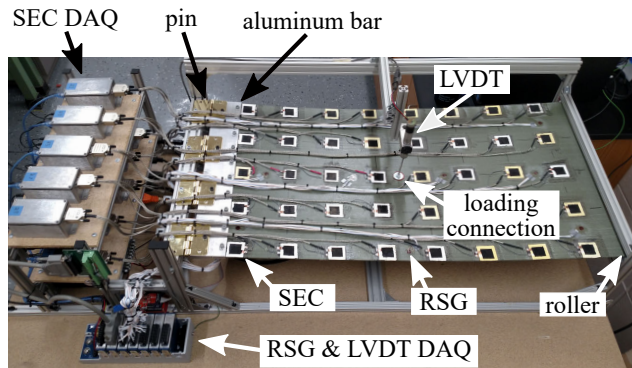


Figure 4. Experimental setup used as the basis for the numerical validation and for generating experimental data used in this work.

393 over the entire distance to create a near continuous strain
 394 distribution as represented by the dashed blue line. Note
 395 that the model goes through the data points used in training
 396 the model and as such this initially estimated strain distribu-
 397 tion can be observed to overestimate the strain at SEC 2 and
 398 underestimate the strain at SEC 3. Now the estimated SEC
 399 signal ($O_i^{\text{SEC,estimated}}$) is obtained from the densely sampled
 400 initial kriging model, and for $i = 3$ (SEC 3), this value is
 401 shown as a blue x in the inset of figure 3. Next the dif-
 402 ference between O_i^{SEC} and $O_i^{\text{SEC,estimated}}$ can be calculated
 403 from Equation 13 and used to adjust the SEC signal used
 404 in training the adjusted kriging model (or the next adjusted
 405 SEC signal in the case of additional iterations) as denoted
 406 in Equation 14. This newly adjusted SEC signal is repre-
 407 sented by an orange filled circle in the inset of figure 3 and
 408 is termed the 1st adjusted SEC signal. This process is re-
 409 peated until the adjusted SEC signal converges to the mea-
 410 sured SEC signal. These adjusted SEC signals, which are
 411 closer to the real strain values at the center of the SEC, can
 412 then be used to generate kriging models that better repro-
 413 duce the shape of the strain topology over the entire area of
 414 interest. For this example, only two iterations are required
 415 to generate a kriging model that shows a marked improve-
 416 ment over the original kriging-estimated strain topography
 417 as shown by the dotted green line in figure 3.

418 4. Methodology

419 This section starts by introducing the experimental test
 420 setup that forms the basis for both the numerical validation
 421 and experimental verification performed in this work.
 422 After, a brief noise quantification study is performed on
 423 an SEC from the experimental setup to provide realistic
 424 noise characteristics for the numerical study. Lastly, the
 425 numerical and experimental studies are presented.

426 4.1. Experimental setup

427 The strain map adjustment algorithm presented in this
 428 work is numerically validated and experimentally verified

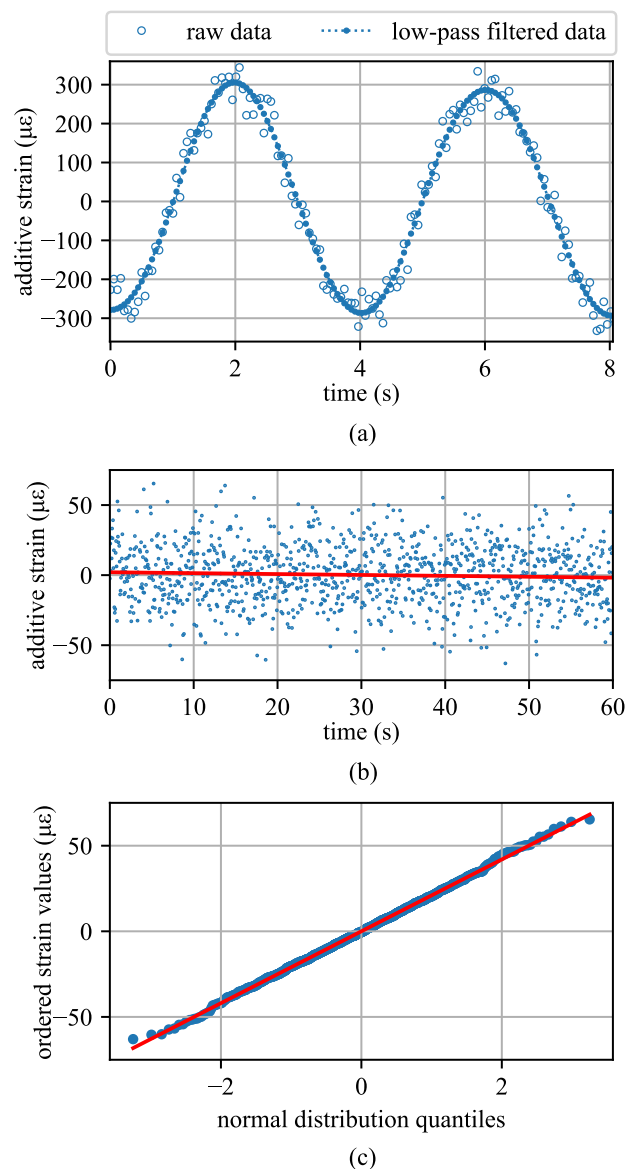


Figure 5. Experimental data for a sensor on the experimental test setup used showing: (a) dynamic response for a sinusoidal input load; (b) static response for a constant load; and (c) q-q plot of the static load compared to a normal distribution.

429 using the configuration shown in figure 4. The numerical
 430 investigation is conducted on an FEA model of the plate
 431 for a variety of sensor layouts. The experimental test setup
 432 consists of a fiberglass plate with a geometry of $500 \times$
 433 $900 \times 2.6 \text{ mm}^3$. The plate is driven by a stepper motor
 434 mounted under the plate and connected to the plate through
 435 a series of mechanical linkages. The left-hand side of the
 436 plate is bolted to an aluminum support ($12.7 \times 76.2 \times 500$
 437 mm^3). This bolted connection forms a rigid connection
 438 that was added to eliminate strain complexities from a
 439 direct connection of the hinge to the fiberglass plate. This
 440 rigid connection is attached to the frame through a pinned
 441 connection. The right-hand side of the plate is restrained in

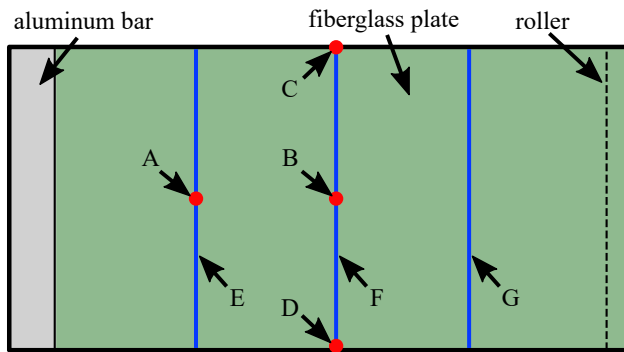


Figure 6. Schematic representation of the experimental plate with the identifiers (A-F) used for annotating the loading points for the ten load cases presented in Table 2.

Table 1. Parameters used in constructing the FEA model.

parameter	value
elements total	298,065
elements type	linear brick
Abaqus element type	C3D8R
elements (aluminum connection)	32,340
elements (fiberglass plate)	265,725
element nodes	8
element integration points	1
Young's Modulus (aluminum)	68.9 GPa
Young's Modulus (fiberglass)	15 GPa
Poisson's ratio (aluminum)	0.33
Poisson's ratio (fiberglass)	0.21
density (aluminum)	2,700 kg/m ³
density (fiberglass)	2,100 kg/m ³
plate dimensions	500 × 900 × 3.18 mm ³

the vertical direction by a roller. This roller consists of two lightly greased rods of diameter 12.7 mm mounted on both the top and bottom of the plate. This experimental setup was previously used in a study related to developing uni-directional strain maps from the SEC-based sensing skin [35].

4.2. SEC noise quantification

A noise signature is extracted from the experimental test setup for the SEC sensor just to the left of the loading point in Figure 4 for the purpose of evaluating the robustness of the strain map adjustment algorithm with respect to noise. The SEC was selected at this location as it experienced a relatively high level of strain during dynamic testing and the length of the cable connecting the SEC sensor to the DAQ is of average length. Figure 5 presents the data for the single sensor under a dynamic (Figure 5(a)) and static (Figure 5(b)) load case. The experimental data for the static load case, sampled at 17 samples per second, was found to have a standard deviation of $\sigma = 32 \mu\epsilon$. The red line

in Figure 5(b) is the best-fit linear regression of the data over the 60-second test. In total, the data was found to drift $4.12 \mu\epsilon$ with r - and p -values of -0.056 and 0.048 respectively. The capability of a normal distribution to effectively estimate the SEC signal noise is demonstrated by the q-q plot presented in Figure 5(c). Therefore, a noise with a normal distribution and a standard deviation of $\sigma = 32 \mu\epsilon$ is deemed appropriate for conducting simulations of the strain map adjustment algorithm with respect to noise.

4.3. Numerical validation

Numerical validation of the strain map adjustment algorithm is performed using 10 load cases of varying complexities applied to an Abaqus FEA model of the experimental test setup [53]. The FEA model was designed to replicate the experimental test setup. In addition to modeling the fiberglass plate, the FEA model also considers the rigid aluminum connection on the left-hand side of the plate. The model is constructed of 298,065 linear brick elements, each with eight-nodes and one integration point. This model configuration was found to have an error of less than 1% when compared to a densely-meshed (1.2 million elements) version of the same FEA model. In the fiberglass plate, nine elements are used through its thickness to prevent shear locking. The plate's connection, pinned on the left-hand side and a roller on the right-hand side, were modeled as ideal connections. The material properties of the fiberglass were obtained experimentally while the properties of the aluminum were taken from the material's data sheet supplied by the distributor. The key parameters of the FEA model are listed in Table 1.

The 10 loading cases are presented using figure 6 and table 2 where figure 6 details the locations of the seven loading location identifiers (A-F) consisting of four loading points (A-D) and three uniform loading conditions (E-G). Table 2 lists the displacement for each of the identifiers for the 10 load cases considered. In the case that a specific location is unused for a load case, its correlating position

Table 2. Displacements associated with the identifiers (A-F) from figure 6 for the 10 loading conditions considered for this study

	displacement (mm)						
	A	B	C	D	E	F	G
load case 1		5					
load case 2	5						
load case 3	0	5					
load case 4			5				
load case 5				5	0		
load case 6					5		
load case 7						5	
load case 8							5
load case 9					5		5
load case 10					5	0	5

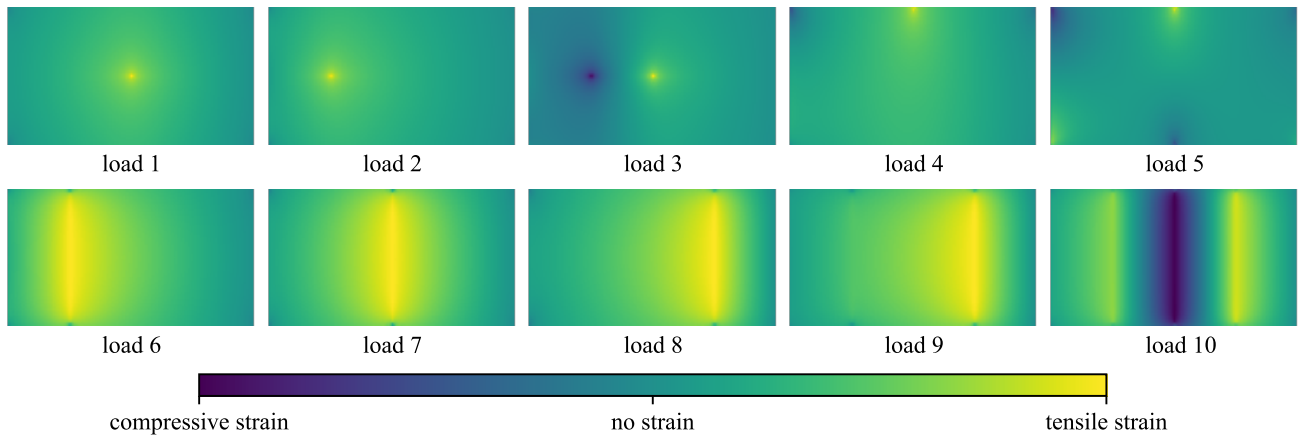


Figure 7. Additive strain maps, generated by the FEA model, for the ten load cases used in the numerical analysis portion of this work. Numerical values for the maximum compressive and tensile strains are listed in Table 3.

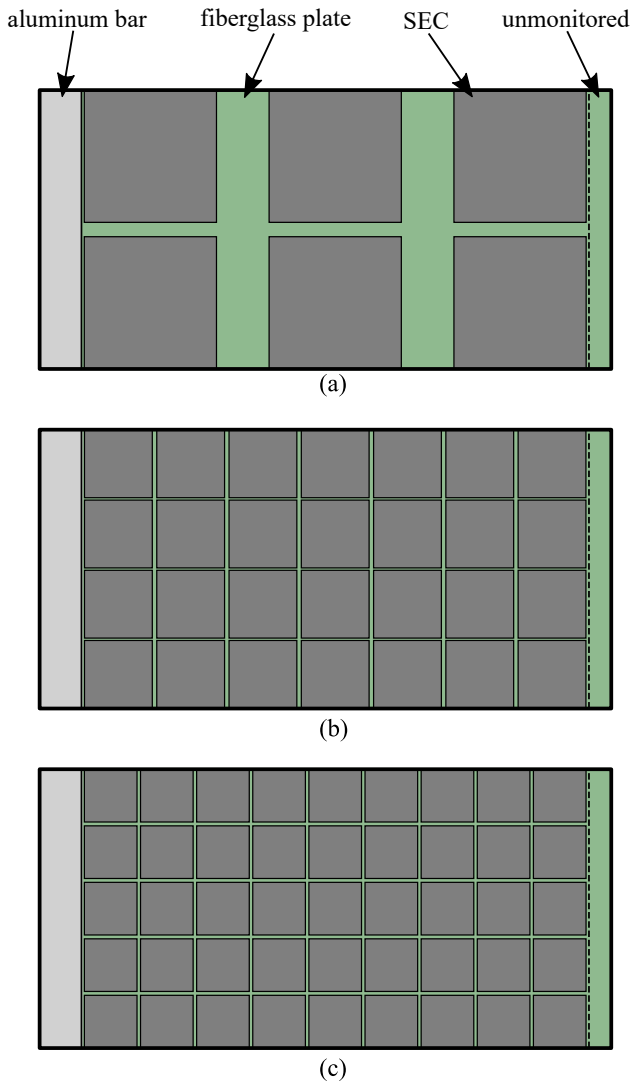


Figure 8. SEC-based sensing skin layouts with: (a) six SECs; (b) 28 SECs; and (c) 45 SECs.

Table 3. Values associated with the maximum compressive and tensile strain for the load cases presented in figure 7.

	maximum compressive strain ($\mu\epsilon$)	maximum tensile strain ($\mu\epsilon$)
load case 1	-1572	1572
load case 2	-1938	1938
load case 3	-7160	7160
load case 4	-1135	1135
load case 5	-1965	1965
load case 6	-1043	1043
load case 7	-907	907
load case 8	-1266	1266
load case 9	-1239	1239
load case 10	-6797	6797

in table 2 is left empty. A displacement of zero denotes a loading point that is fixed at 0 mm of displacement. The strain maps produced for these 10 load cases are shown in figure 7. These load cases were selected to develop strain maps that produced varying amounts of asymmetry and strain map complexity. For each load case, the strain maps are normalized to either their maximum compressive or tensile strain values to help the visualization of results such that the no strain condition is the same color for each plot. The values associated with the maximum compressive and tensile strain for the load cases are listed in table 3.

The numerical validation also investigated the effect of changing sensor densities on the accuracy of both the traditional kriging and adjusted kriging strain maps. To do this, an algorithm was formulated that covered the monitored area of the fiberglass plate with an evenly spaced grid of square SEC sensors. This algorithm started with six sensors and progressively added square sensors to the fiberglass plate by reducing the size of each individual sensor. Every combination of square sensors arranged in a rectangular grid formed from six to 500 sensors was

498
499
500
501
502
503
504
505
506
507
508
509
510
511
512
513
514
515
516
517
518

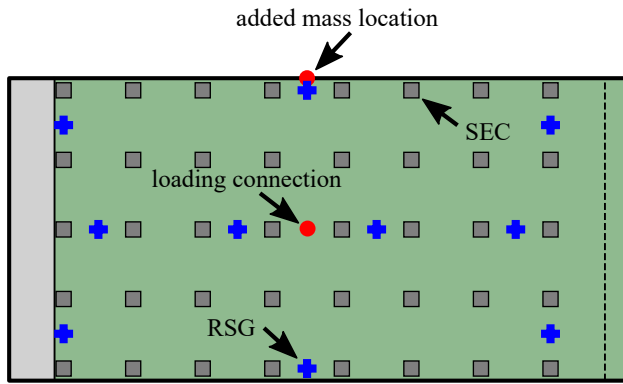


Figure 9. SEC and RSG layout of the experimental test setup used for experimental validation.

519 considered, with a total of 39 different grid configurations
 520 considered. Figure 8 shows the SEC sensor layouts for three
 521 different sensor densities. As the strain map adjustment
 522 algorithm seeks to only update the strain value at the center
 523 of each SEC, the spaces between the SECs do not have
 524 a direct effect on the strain map interpolations. However,
 525 this unmonitored area does have a secondary effect on
 526 the performance of the algorithm as an area that is not
 527 monitored by a sensor will not be fused into the adjusted
 528 additive strain map. For uniformity, this work considers
 529 only SEC sensors of a square geometry. The investigation
 530 of other dense sensor network configurations, including
 531 those with non-uniform sensor densities, geometries, and
 532 sizes, are beyond the scope of this introductory work.

533 4.4. Experimental verification

534 The experimental verification for the strain map adjustment
 535 algorithm was performed using a network of 40 SECs
 536 deployed as a grid onto the fiberglass plate. The layout
 537 of these SECs is presented in figure 9. In addition to the
 538 40 SECs, 20 RSGs were deployed onto the fiberglass plate
 539 for the purpose of validating the strain map adjustment
 540 algorithm at various locations on the plate. The RSGs
 541 (model #FCA-5-350-11-3LJBT, manufactured by Tokyo
 542 Sokki Kenkyujo) were deployed in pairs, each individually
 543 measuring ε_x and ε_y . The 40 SECs were deployed in a 5
 544 $\times 8$ grid array, each monitoring an area of 38×38 mm².
 545 The DAQ system consists of 10 custom-built capacitance
 546 measurement devices (annotated as SEC DAQ in figure 4)
 547 that also generate an active shield for the cable that removes
 548 the parasitic capacitance found in the cable. In addition
 549 to these devices, a chassis (cDAQ-9178, manufactured by
 550 National Instruments) was used to hold three quarter bridge
 551 analog input (NI-9236) modules for measuring the RSGs,
 552 an analog input module (NI-9205) for measuring the LVDT,
 553 and a digital output module (NI-9472) for sourcing a trigger
 554 to ensure the SEC and RSG data is sampled simultaneously.
 555 Additionally, an LVDT (model #0244, manufactured by

Trans-Tek) was mounted to the plate to record the plates
 center displacement. All the data sources were measured
 at 17 samples per second. Lastly, to remove the high-
 frequency noise found in the SEC signal, a fifth-order
 Butterworth filter with a cutoff frequency of 10 Hz was
 used. The effects of this filtering can be seen in figure 5(a).
 No filtering was needed for either the RSG or LVDT data.

The experimental validation considered two experi-
 mental load cases. First, load case 1 (similar to load case
 1 in the numerical investigation) is used to verify the strain
 map adjustment algorithm for a relatively simple load case.
 This load case is produced at the center of the plate by the
 stepper motor located under the plate. The plate is displaced
 5 mm from its initial condition harmonically at 0.25 Hz.
 Second, an asymmetric load is generated to verify the strain
 map adjustment algorithm under a more complex loading
 condition. To generate this asymmetric load, a 0.5 kg mass
 is added at the center of the plate along its top edge (see
 Figure 9) then the plate is excited using the stepper motor
 in the same manner as load case 1. For both cases, the ex-
 perimental data is investigated over two complete cycles.

5. Results

This section presents the results from both the numerical
 and experimental studies. First, a detailed evaluation of
 the strain map adjustment algorithm for load case 4 is
 presented, followed by a discussion on the results for all ten
 load cases. Lastly, the experimental results are discussed.

5.1. Numerical validation

Results for the strain map adjustment algorithm for load
 case 4, monitored with 28 SECs as shown in figure 8(b),
 are presented in figure 10. The combination of load case 4
 with 28 SECs was selected due to its capability to demon-
 strate both portions of the strain field where the strain map
 adjustment algorithm improves the accuracy of the strain
 map (i.e. near the load case) and portions where its benefit
 is less obvious (i.e. portions the strain topography that
 are relatively simple). To expand, figure 10 presents both
 the plate's real strain map and its kriging-estimated strain
 maps using the traditional kriging method (figure 10(a))
 and the strain map adjustment algorithm (figure 10(b)).
 Figure 10(c) reports the RMSE error between the real strain
 map and that estimated using the strain map adjustment
 algorithm over each successive iteration of the algorithm.
 In figure 10(c) the initial condition is the strain map
 generated using a traditional kriging method (figure 10(a))
 and therefore does not incorporate the sensor geometry into
 the strain map interpolation. Conversely, the strain map for
 iteration 16 (figure 10(b)) incorporates the sensor geometry
 into the reconstructed strain maps. The inset in figure
 10(c) shows the reduction in strain map reconstruction error
 (measured as $\mu\varepsilon$) by the strain map adjustment algorithm
 (figure 10(b)) over the traditional kriging method (figure

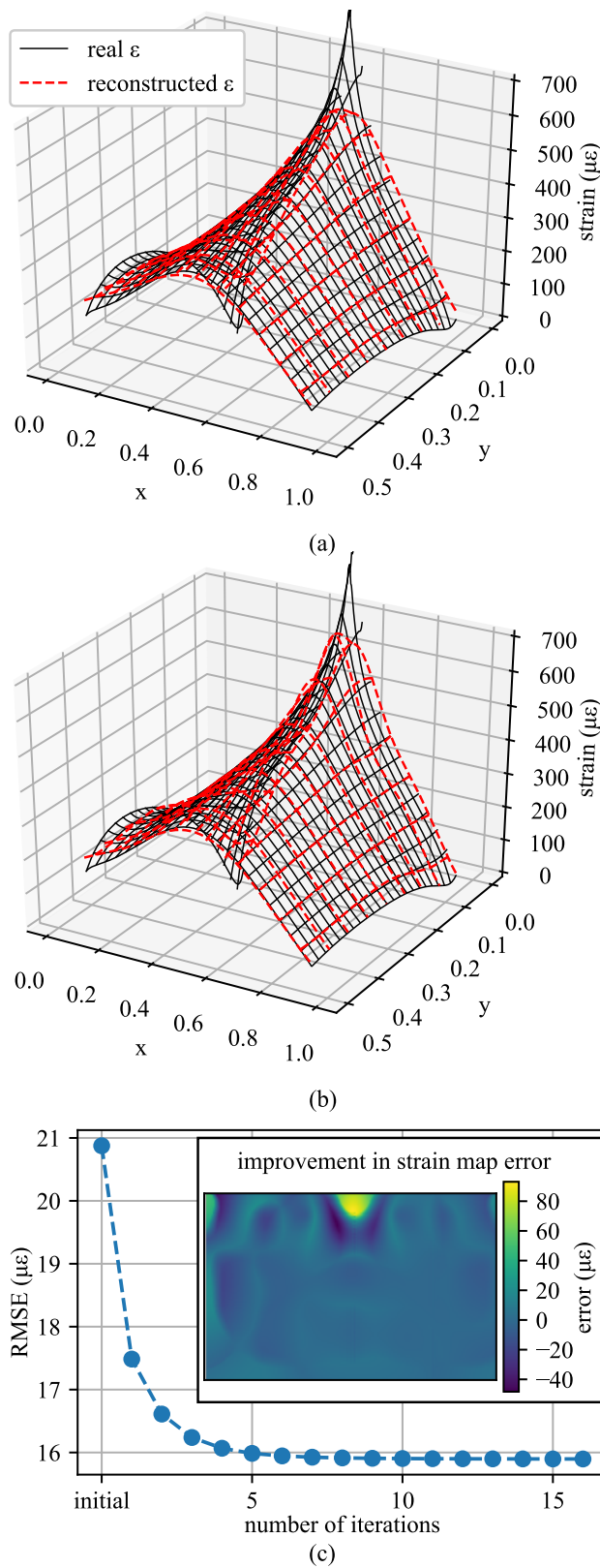


Figure 10. Strain maps generated for load case 4: (a) using the traditional kriging method; (b) using the strain map adjustment algorithm; and (c) showing the RMSE as a function of number of iterations for the strain map adjustment algorithm where the inset shows the improvement in strain between the traditional kriging method and the proposed algorithm.

10(a)). The strain map adjustment algorithm generates a considerable improvement near the loading point at the top center of the plate where the traditional kriging method underestimates the real strain value. Furthermore, the algorithm generally improves the accuracy of the strain map over the entire plate.

Figure 11 reports the results for the ten cases used in the numerical validation in terms of the root mean squared error (RMSE) where the error is measured at every point of the strain map. Results are reported for the RMSE from both the traditional kriging method and for the strain map adjustment algorithm. These results are reported with and without noise added to the system. Overall, the strain maps developed using the strain map adjustment algorithm have less error than those developed using the traditional method. A few notable results for some specific load cases are as follows. First, it should be noted that in every load case considered for the no-noise conditions the adjusted strain maps are capable of achieving a level of error that would require far more sensors than if the strain map adjustment algorithm was not used. When noise was added to the sensor signal and for loading conditions that developed low levels of strain (e.g. load cases 1, 4, and 7), the benefit of using the strain map adjustment algorithm for a given number of SECs was reduced but never worse than the traditional kriging method's error levels. Next, it can be noticed that load cases 4 and 5 experience an increase in error for an increase in the number of sensors deployed in the dense sensor network before leveling out once a certain number of sensors are used. This increase in RMSE for load cases 4 and 5 come from the very center of the plate where the kriging method underestimates the peak strain value due to sensors being positioned right on top of this high strain concentration. However, in both of these cases, the strain map adjustment algorithm is capable of compensating for this concentrated strain location.

5.2. Experimental verification

The experimental results for the 40 sensors deployed on the experimental test setup are presented in figure 12. The strain maps in figure 12(a) report the full-field strain maps developed using the strain map adjustment algorithms for both load cases. For the experimental study the RMSE is measured at the 20 RSG locations on the plate. The RSGs are used for this task due to their higher accuracy when compared to the SECs, and capability to measure the additive strain at any location when their signals are added together. As expected, the RMSE for both load cases generally increases when the displacement is increasing and is near either its maximum upward or maximum downward displacement. Load case 1 (figure 12(b)) does report lower error values than load case 2 12(c)). This increase in the error for load case 2 is to be expected given the general increase in the complexity of the strain topography for load case 2, as seen in figure 12(a). Additionally, for two brief

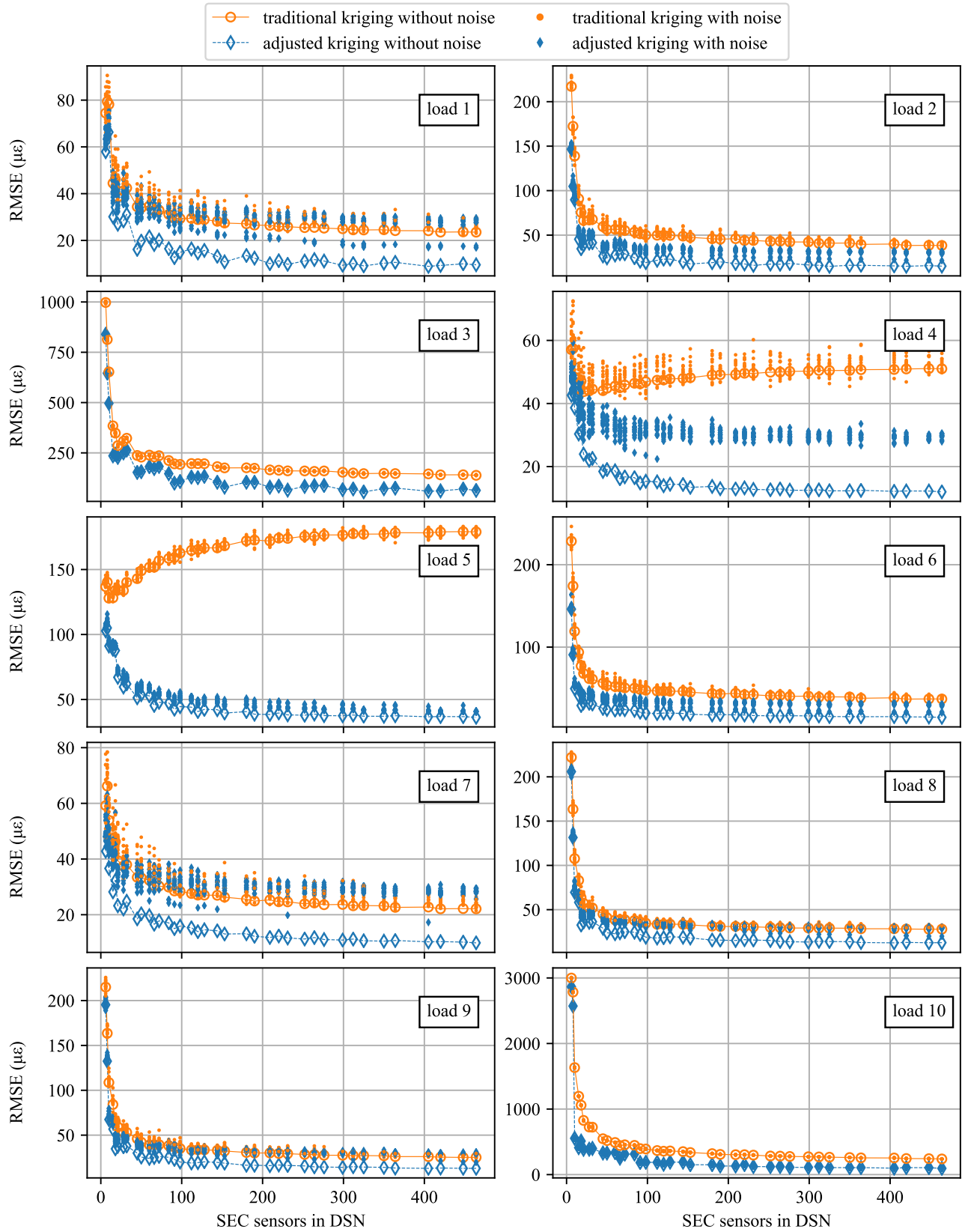


Figure 11. RMSE results for both the traditional kriging and the adjusted kriging methods for all ten load cases, considered both with and without noise.

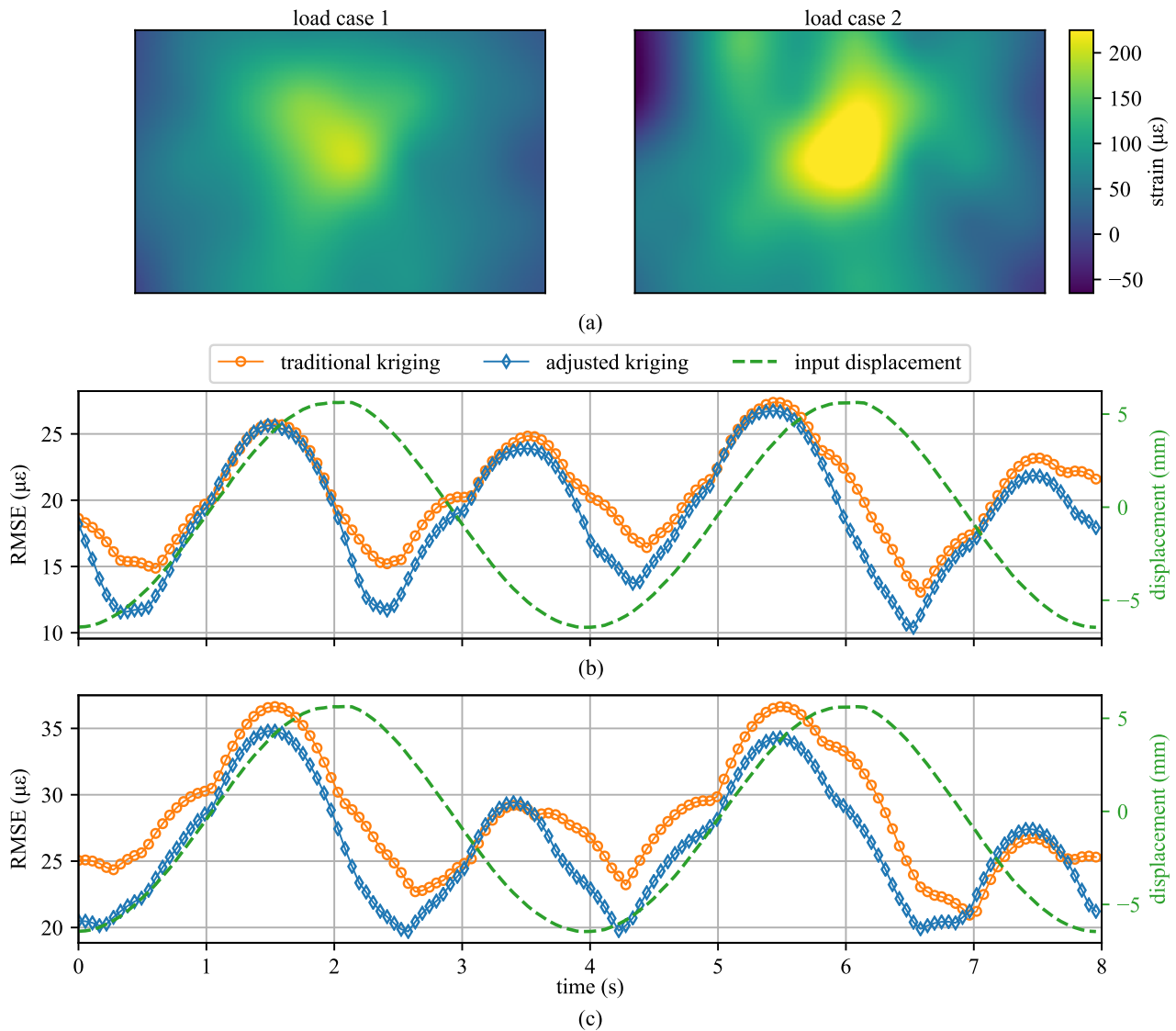


Figure 12. Temporal RMSE results for the 0.25 Hz loading condition under the experimental: (a) load case 1; and (b) load case 2. This figure appears as a video in the online version of this paper.

662 moments in load case 2 around 3.4 and 7.4 seconds, the
 663 adjusted strain map reports a higher level of error than those
 664 generated using the traditional kriging methods. This can
 665 be attributed to the relatively small number of RSG gauges
 666 used for quantifying the error of the full-field strain maps.

667 6. Conclusion

668 This work proposed an algorithm that fuses the locations of
 669 strain sensors, their signals, and the geometry of a network
 670 of sensor constituting a sensing skin into an approximated
 671 full-field strain map. These sensors, termed the soft
 672 elastomeric capacitors (SECs), are a large-area electronic
 673 that are capable of covering large areas at low costs. Given
 674 that each SEC measures the summation of a structure's
 675 orthogonal strains (i.e. $\epsilon_x + \epsilon_y$), the SECs deployed in

a network configuration are capable of reproducing the
 full-field additive strain map of a structure. These full-
 field strain maps can then be used to extract physics-based
 features for real-time condition assessment. Examples of
 the physics-based features include changes in strain maps
 and deflection shapes.

The proposed algorithm improves the quality of these
 full-field strain maps by fusing the sensor size into a
 traditional strain field interpolation that only uses the
 sensor location and signal. This work used kriging as
 the interpolation method. However, other interpolation
 methods including cubic splines and radial bias functions
 could also be used. The improvement in the additive
 full-field strain map generation is accomplished through
 iterative adjustments to the measured SEC signal used as
 the input to the kriging model until the measured SEC signal

676
677
678
679
680
681
682
683
684
685
686
687
688
689
690
691

692 matches the SEC signal estimated using the kriging model.
 693 Therefore, the newly proposed algorithm fuses data from
 694 the SEC's location, signal, and geometry to produce a full-
 695 field strain map. Results from numerical and experimental
 696 investigations show that the proposed strain map adjustment
 697 algorithm is capable of generating improved full-field strain
 698 maps over those produced using the traditional kriging
 699 method.

700 Acknowledgements

701 This work was in part supported by the National Science
 702 Foundation Grant Nos. CNS-1566579 and ECCS-1611333.
 703 This work was also partly supported by the National
 704 Science Foundation Grant No. 1069283, which supports
 705 the activities of the Integrative Graduate Education and
 706 Research Traineeship (IGERT) in Wind Energy Science,
 707 Engineering and Policy (WESEP) at Iowa State University.
 708 Their support is gratefully acknowledged. Any opinions,
 709 findings, and conclusions or recommendations expressed in
 710 this material are those of the authors and do not necessarily
 711 reflect the views of the National Science Foundation.

712 References

713 [1] Jerome P. Lynch, Charles R. Farrar, and Jennifer E. Michaels.
 714 Structural health monitoring: technological advances to practical
 715 implementations [scanning the issue]. *Proceedings of the IEEE*,
 716 104(8):1508–1512, aug 2016.
 717 [2] Yao Yao, Shue-Ting Ellen Tung, and Branko Glisic. Crack detection
 718 and characterization techniques-an overview. *Structural Control*
 719 *and Health Monitoring*, 21(12):1387–1413, mar 2014.
 720 [3] Daniele Posenato, Francesca Lanata, Daniele Inaudi, and Ian F.C.
 721 Smith. Model-free data interpretation for continuous monitoring
 722 of complex structures. *Advanced Engineering Informatics*,
 723 22(1):135–144, jan 2008.
 724 [4] Merit Enckell, Branko Glisic, Frank Myrvoll, and Benny Bergstrand.
 725 Evaluation of a large-scale bridge strain, temperature and crack
 726 monitoring with distributed fibre optic sensors. *Journal of Civil*
 727 *Structural Health Monitoring*, 1(1-2):37–46, mar 2011.
 728 [5] Jerome Peter Lynch, Arvind Sundararajan, Kincho H Law, Anne S
 729 Kiremidjian, and Ed Carryer. Embedding damage detection
 730 algorithms in a wireless sensing unit for operational power
 731 efficiency. *Smart Materials and Structures*, 13(4):800–810, jun
 732 2004.
 733 [6] Marcus Perry, Jack McAlorum, Grzegorz Fusiek, Pawel Niewczas,
 734 Iain McKeeman, and Tim Rubert. Crack monitoring of
 735 operational wind turbine foundations. *Sensors*, 17(8):1925, aug
 736 2017.
 737 [7] Jarkko Tikka, Risto Hedman, and A Silijander. Strain gauge
 738 capabilities in crack detection. In *4th International Workshop on*
 739 *Structural Health Monitoring*, pages 15–17, 2003.
 740 [8] S-T Tung, Y Yao, and B Glisic. Sensing sheet: the sensitivity
 741 of thin-film full-bridge strain sensors for crack detection
 742 and characterization. *Measurement Science and Technology*,
 743 25(7):075602, may 2014.
 744 [9] H M Lee, J M Kim, K Sho, and H S Park. A wireless vibrating wire
 745 sensor node for continuous structural health monitoring. *Smart*
 746 *Materials and Structures*, 19(5):055004, mar 2010.
 747 [10] Yunmiao Wang, Jianmin Gong, Bo Dong, Dorothy Y. Wang, Tyler J.
 748 Shillig, and Anbo Wang. A large serial time-division multiplexed
 749 fiber bragg grating sensor network. *Journal of Lightwave*
 750 *Technology*, 30(17):2751–2756, sep 2012.

[11] Kenneth J. Loh, Tsung-Chin Hou, Jerome P. Lynch, and Nicholas A.
 751 Kotov. Carbon nanotube sensing skins for spatial strain
 752 and impact damage identification. *Journal of Nondestructive*
 753 *Evaluation*, 28(1):9–25, mar 2009.
 754 [12] P. Hua, E.J. Woo, J.G. Webster, and W.J. Tompkins. Finite element
 755 modeling of electrode-skin contact impedance in electrical
 756 impedance tomography. *IEEE Transactions on Biomedical*
 757 *Engineering*, 40(4):335–343, apr 1993.
 758 [13] Milad Hallaji, Aku Seppänen, and Mohammad Pour-Ghaz. Elec-
 759 trical impedance tomography-based sensing skin for quantitative
 760 imaging of damage in concrete. *Smart Materials and Structures*,
 761 23(8):085001, jun 2014.
 762 [14] Yunfeng Zhang. In situ fatigue crack detection using piezoelectric
 763 paint sensor. *Journal of Intelligent Material Systems and*
 764 *Structures*, 17(10):843–852, oct 2006.
 765 [15] T.-C. Hou and J. P. Lynch. Electrical impedance tomographic meth-
 766 ods for sensing strain fields and crack damage in cementitious
 767 structures. *Journal of Intelligent Material Systems and Struc-*
 768 *tures*, 20(11):1363–1379, sep 2008.
 769 [16] Liliana Borcea. Electrical impedance tomography. *Inverse*
 770 *Problems*, 18(6):R99–R136, oct 2002.
 771 [17] Austin Downey, Antonella D'Alessandro, Micah Baquera, En-
 772 rique García-Macías, Daniel Rolfes, Filippo Ubertini, Simon
 773 Laflamme, and Rafael Castro-Triguero. Damage detection, local-
 774 ization and quantification in conductive smart concrete structures
 775 using a resistor mesh model. *Engineering Structures*, 148:924 –
 776 935, 2017.
 777 [18] Austin Downey, Antonella D'Alessandro, Filippo Ubertini, and Si-
 778 mon Laflamme. Automated crack detection in conductive smart-
 779 concrete structures using a resistor mesh model. *Measurement*
 780 *Science and Technology*, dec 2017.
 781 [19] Bing Pan, Kemao Qian, Huimin Xie, and Anand Asundi. Two-
 782 dimensional digital image correlation for in-plane displacement
 783 and strain measurement: a review. *Measurement Science and*
 784 *Technology*, 20(6):062001, apr 2009.
 785 [20] Donghyeon Ryu and Kenneth J Loh. Strain sensing using photocur-
 786 rent generated by photoactive p3ht-based nanocomposites. *Smart*
 787 *Materials and Structures*, 21(6):065016, may 2012.
 788 [21] Ana Claudia Arias, J. Devin MacKenzie, Iain McCulloch, Jonathan
 789 Rivnay, and Alberto Salleo. Materials and applications for large
 790 area electronics: Solution-based approaches. *Chemical Reviews*,
 791 110(1):3–24, jan 2010.
 792 [22] J A Paradiso, J Lifton, and M Broxton. Sensate media — multimodal
 793 electronic skins as dense sensor networks. *BT Technology*
 794 *Journal*, 22(4):32–44, oct 2004.
 795 [23] Branko Glisic, Yao Yao, Shue-Ting E. Tung, Sigurd Wagner,
 796 James C. Sturm, and Naveen Verma. Strain sensing sheets for
 797 structural health monitoring based on large-area electronics and
 798 integrated circuits. *Proceedings of the IEEE*, 104(8):1513–1528,
 799 aug 2016.
 800 [24] Yingzhe Hu, Warren S. A. Rieutort-Louis, Josue Sanz-Robinson,
 801 Liechao Huang, Branko Glisic, James C. Sturm, Sigurd Wagner,
 802 and Naveen Verma. Large-scale sensing system combining large-
 803 area electronics and CMOS ICs for structural-health monitoring.
 804 *IEEE Journal of Solid-State Circuits*, 49(2):513–523, feb 2014.
 805 [25] Inpil Kang, Mark J Schulz, Jay H Kim, Vesselin Shanov, and
 806 Donglu Shi. A carbon nanotube strain sensor for structural health
 807 monitoring. *Smart Materials and Structures*, 15(3):737–748, apr
 808 2006.
 809 [26] Kenneth J Loh, Junhee Kim, Jerome P Lynch, Nadine Wong Shi
 810 Kam, and Nicholas A Kotov. Multifunctional layer-by-
 811 layer carbon nanotube–polyelectrolyte thin films for strain and
 812 corrosion sensing. *Smart Materials and Structures*, 16(2):429–
 813 438, feb 2007.
 814 [27] Colin Robert, Jean François Feller, and Mickaël Castro. Sensing
 815 skin for strain monitoring made of PC–CNT conductive polymer
 816 nanocomposite sprayed layer by layer. *ACS Applied Materials &*
 817 *Interfaces*, 4(7):3508–3516, jun 2012.
 818 [28] AR Burton, JP Lynch, M Kurata, and KH Law. Fully integrated
 819 carbon nanotube composite thin film strain sensors on flexible
 820

- substrates for structural health monitoring. *Smart Materials and Structures*, 26(9), 2017.
- [29] Sida Luo, Phong Tran Hoang, and Tao Liu. Direct laser writing for creating porous graphitic structures and their use for flexible and highly sensitive sensor and sensor arrays. *Carbon*, 96:522–531, jan 2016.
- [30] Yuzheng Zhang, Nickolas Anderson, Scott Bland, Steven Nutt, Gregory Jursich, and Shiv Joshi. All-printed strain sensors: Building blocks of the aircraft structural health monitoring system. *Sensors and Actuators A: Physical*, 253:165–172, jan 2017.
- [31] Simon Laflamme, Matthias Kolloosche, Jerome J. Connor, and Guggi Kofod. Robust flexible capacitive surface sensor for structural health monitoring applications. *Journal of Engineering Mechanics*, 139(7):879–885, jul 2013.
- [32] Austin Downey, Simon Laflamme, and Filippo Ubertini. Durability assessment of soft elastomeric capacitor skin for shm of wind turbine blades. In H. Felix Wu, Andrew L. Gyekenyesi, Peter J. Shull, and Tzu-Yang Yu, editors, *Nondestructive Characterization and Monitoring of Advanced Materials, Aerospace, and Civil Infrastructure 2017*. SPIE, apr 2017.
- [33] Simon Laflamme, Hussam S. Saleem, Bharath K. Vasani, Randall L. Geiger, Degang Chen, Michael R. Kessler, and Krishna Rajan. Soft elastomeric capacitor network for strain sensing over large surfaces. *IEEE/ASME Transactions on Mechatronics*, 18(6):1647–1654, dec 2013.
- [34] Simon Laflamme, Filippo Ubertini, Hussam Saleem, Antonella D’Alessandro, Austin Downey, Halil Ceylan, and Annibale Luigi Materazzi. Dynamic characterization of a soft elastomeric capacitor for structural health monitoring. *Journal of Structural Engineering*, 141(8):04014186, aug 2015.
- [35] Mohammadkazem Sadoughi, Austin Downey, Jin Yan, Chao Hu, and Simon Laflamme. Reconstruction of unidirectional strain maps via iterative signal fusion for mesoscale structures monitored by a sensing skin. *Mechanical Systems and Signal Processing*, 2018 (under revision).
- [36] Austin Downey, Simon Laflamme, and Filippo Ubertini. Reconstruction of in-plane strain maps using hybrid dense sensor network composed of sensing skin. *Measurement Science and Technology*, 27(12):124016, nov 2016.
- [37] Xiangxiong Kong, Jian Li, William Collins, Caroline Bennett, Simon Laflamme, and Hongki Jo. A large-area strain sensing technology for monitoring fatigue cracks in steel bridges. *Smart Materials and Structures*, 26(8):085024, jul 2017.
- [38] Simon Laflamme, Liang Cao, Eleni Chatzi, and Filippo Ubertini. Damage detection and localization from dense network of strain sensors. *Shock and Vibration*, 2016:1–13, 2016.
- [39] Austin Downey, Simon Laflamme, and Filippo Ubertini. Experimental wind tunnel study of a smart sensing skin for condition evaluation of a wind turbine blade. *Smart Materials and Structures*, Oct 2017.
- [40] J. Park and I. W. Sandberg. Universal approximation using radial-basis-function networks. *Neural Computation*, 3(2):246–257, jun 1991.
- [41] Carl De Boor, Carl De Boor, Etats-Unis Mathématicien, Carl De Boor, and Carl De Boor. *A practical guide to splines*, volume 27. Springer-Verlag New York, 1978.
- [42] Carl Edward Rasmussen. *Gaussian Processes in Machine Learning*. Springer Berlin Heidelberg, 2004.
- [43] R.E. Day. The role of titanium dioxide pigments in the degradation and stabilisation of polymers in the plastics industry. *Polymer Degradation and Stability*, 29(1):73–92, jan 1990.
- [44] H. Saleem, M. Thunga, M. Kolloosche, M.R. Kessler, and S. Laflamme. Interfacial treatment effects on behavior of soft nano-composites for highly stretchable dielectrics. *Polymer*, 55(17):4531–4537, aug 2014.
- [45] Carbon black. In John Wiley & Sons Inc, editor, *Kirk-Othmer Encyclopedia of Chemical Technology*. John Wiley & Sons, Inc., dec 2000.
- [46] A.N. Wilkinson, M.L. Clemens, and V.M. Harding. The effects of SEBS-g-maleic anhydride reaction on the morphology and properties of polypropylene/PA6/SEBS ternary blends. *Polymer*, 45(15):5239–5249, jul 2004.
- [47] Bobak Shahriari, Kevin Swersky, Ziyu Wang, Ryan P. Adams, and Nando de Freitas. Taking the human out of the loop: A review of bayesian optimization. *Proceedings of the IEEE*, 104(1):148–175, jan 2016.
- [48] Tomislav Hengl, Gerard B.M. Heuvelink, and Alfred Stein. A generic framework for spatial prediction of soil variables based on regression-kriging. *Geoderma*, 120(1-2):75–93, may 2004.
- [49] Matthew J. Tonkin and Steven P. Larson. Kriging water levels with a regional-linear and point-logarithmic drift. *Ground Water*, 40(2):185–193, mar 2002.
- [50] Peter K. Kitanidis. *Introduction to geostatistics: applications in hydrogeology*. Cambridge University Press, 1997.
- [51] M.A. Oliver and R. Webster. A tutorial guide to geostatistics: Computing and modelling variograms and kriging. *CATENA*, 113:56–69, feb 2014.
- [52] mjziebarth basaks rth, bsmurphy. Pykrige: Kriging toolkit for python, 2018.
- [53] Hibbit, Karlsson, and Sorensen. *ABAQUS/Standard Analysis User’s Manual*. Hibbit, Karlsson, Sorensen Inc., USA, 2007.